Mon. Not. R. Astron. Soc. **000**, 1–24 (2004) Printed 6 June 2005 (MN LATEX style file v2.2)

Density–potential pairs for spherical stellar systems with Sérsic light–profiles and (optional) power–law cores

Balša Terzić[1,2] and Alister W. Graham[3]
[1]*Department of Physics, Northern Illinois University, DeKalb, IL 60115, USA*
[2]*Corresponding Author: bterzic@nicadd.niu.edu*
[3]*Research School of Astronomy and Astrophysics, Australian National University Private Bag, Weston Creek PO, ACT 2611, Canberra, Australia*

Received 2005 April 13; Accepted 2005 December 31

ABSTRACT

Popular models for describing the luminosity–density profiles of dynamically hot stellar systems (e.g., Jaffe, Hernquist, Dehnen) were constructed with the desire to match the deprojected form of an $R^{1/4}$ light–profile. Real galaxies, however, are now known to have a range of different light–profile shapes that scale with mass. Consequently, the above models have implicit limitations, and this is illustrated here through their application to a number of real galaxy density profiles. On the other hand, the analytical density profile given by Prugniel & Simien (1997) closely matches the deprojected form of Sérsic $R^{1/n}$ light–profiles — including deprojected exponential light–profiles. It is thus applicable for describing bulges in spiral galaxies, dwarf elliptical galaxies, and both ordinary and giant elliptical galaxies. Here we provide simple equations, in terms of elementary and special functions, for the gravitational potential and force associated with this density profile. Furthermore, to match galaxies with partially depleted cores, and better explore the supermassive black hole / galaxy connection, we have added a power–law core to this density profile and derived similar expressions for the potential and force of this hybrid profile. Expressions for the mass and velocity dispersion, assuming isotropy, are also given. These spherical models may also prove appropriate for describing the dark matter distribution in halos formed from ΛCDM cosmological simulations.

Key words: galaxies: elliptical and lenticular, cD – galaxies: kinematics and dynamics – galaxies: nuclei – galaxies: structure – stellar dynamics

1 INTRODUCTION

Both elliptical galaxies and the bulges of disk galaxies, hereafter collectively referred to as "bulges", possess a range of light–profile "shapes" that are well described by Sérsic's (1963, 1968) $R^{1/n}$ model (e.g., Caon, Capaccioli & D'Onofrio 1993; Young & Currie 1994; Graham et al. 1996; Graham 2001; Balcells et al. 2003). This model is a generalisation of de Vaucouleurs' (1948, 1959) $R^{1/4}$ model which is known to be only appropriate for a subset of elliptical galaxies having $M_B \sim -21$ mag (e.g., Kormendy & Djorgovski 1989; Graham & Guzmán 2003). The $R^{1/4}$ model's limitation lies in the fact that it has only two parameters: a radial scale and a surface brightness scale. The actual curvature, or "shape", of every $R^{1/4}$ model is the same.

This restriction has carried over into computer simulations of "bulges". This is because the popular models that are used for describing the luminosity–density profiles of bulges, such as those from Jaffe (1983), Hernquist (1990), and Dehnen (1993, see also Tremaine et al. 1994), were created in order to reproduce an $R^{1/4}$ light–profile when projected. All three of these density models have exactly the same outer profile slope, declining with radius as r^{-4}. Consequently, these models are limited in their ability to a) simulate the range of observed galaxy structures and b) quantify the evolution of these structures.

Over the past two decades it has also become apparent that the most luminous ($M_B < -20.5$ mag) elliptical galaxies have partially–depleted stellar–cores (Kormendy 1985; Lauer 1985; Ferrarese et al. 1994; Lauer et al. 1995; Gebhardt et al. 1996). On the other hand, the less luminous elliptical galaxies, sometimes referred to as "power–law" galaxies, have continuously curving Sérsic profiles that continue all the way in to the resolution limit of *HST* images (Trujillo et al. 2004). A promising explanation, albeit not the only one proffered, for the depleted cores is that the giant galaxies formed from the dissipationless merger of two or more fainter elliptical galaxies. The subsequent gravitational ejection of stars by the inwardly spiralling supermassive black holes (SMBHs) — from the progenitor galaxies – scours out the core of the new galaxy (e.g., Begelman, Blandford & Rees 1980; Makino & Ebisuzaki 1996; Faber et al. 1997; Milosavljević & Merritt 2001, 2005; Graham 2004). Furthermore, fundamental connections have been found between the SMBH mass and a bulge's: *(i)* magnitude (Magorrian et al. 1998; McLure & Dunlop 2002; Erwin, Graham & Caon 2002), *(ii)* light–profile shape (Graham et al. 2001, 2003a) and *(iii)* kinematics (Ferrarese & Merritt 2000, Gebhardt et al. 2000).

Given the above connections, it is obviously important to have models that are able to unite properly the domain of the black hole with the rest of the galaxy. In this paper we present a modification of Prugniel & Simien's (1997) density model that already matches the observed range of 'outer' profile shapes; our modification allows one to additionally model partially depleted cores. Moreover, and importantly, we also derive exact expressions for the potential and force in terms of (fast–to–compute) elementary functions, making it possible for simulations to explore the influence of cores and differing profile shapes. By setting the size of the partially depleted core to zero, the equations for the potential and force are applicable to the original Prugniel–Simien density profile, for which no previous expressions existed.

In subsection 2.1 we introduce the density model, complete with power–law core, while subsection 2.2 provides the equations for the potential and force. Expressions for the projection of the density model can be found in subsection 2.3. In section 3 we fit a number of popular density models to the luminosity–density profiles of real galaxies and compare the results with the fit from the Prugniel–Simien density model and our modification of this model. A discussion of relevant issues is given in section 4, and section 5 provides a summary of the main results. Appendix A provides the derivation for various expressions pertaining to the velocity structure of the density profiles, including the circular velocity, spatial and line–of–sight velocity dispersion. Appendix B provides the derivation of the equations given in section 2.

2 THE MODEL

In this section we introduce a family of expressions associated with the spatial density profiles of spherical stellar systems having Sérsic-like profiles with optional power–law cores. We derive *exact* expressions for the potential and force and outline how the corresponding surface brightness can be computed numerically (see Fig.1). With computer processing speed

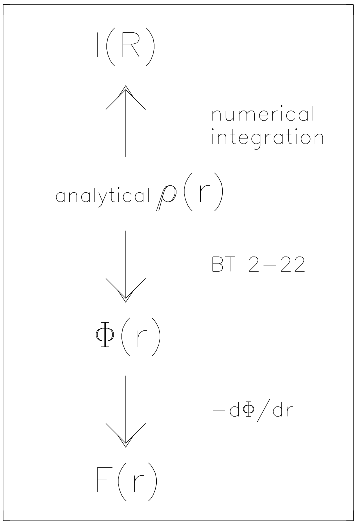

Figure 1. Flow chart for the density model: the projection of the analytically prescribed density is computed numerically, while the potential and force are obtained *exactly.* BT 2–22 refers to Binney & Tremaine (1987, their equation 2–22).

in mind, in addition to the pressing need for more flexible galaxy models, the equations consist only of analytical terms and simple elementary functions.

For the sake of parameter identification, we first introduce Sérsic's (1963, 1968) model for describing the projected, radial intensity profiles of galaxies, such that

$$I(R) = I_0 \mathrm{e}^{-b(R/R_\mathrm{e})^{1/n}}, \qquad (1)$$

where I_0 is the central intensity and R_e is the (projected) effective half–light radius. The parameter n describes the curvature of the profile (see, e.g., Ciotti 1991). The term b is not a parameter, but instead a function of n and chosen to ensure R_e contains half the (projected) galaxy light. It is obtained by solving the equation $\Gamma(2n) = 2\,\gamma(2n, b)$, where

$$\Gamma(a) = \int_0^\infty \mathrm{e}^{-t} t^{a-1} \mathrm{d}t \qquad \text{and} \qquad \gamma(a,x) = \int_0^x \mathrm{e}^{-t} t^{a-1} \mathrm{d}t, \quad a > 0 \qquad (2)$$

are the complete and incomplete gamma functions, respectively. Although we have chosen to numerically compute the exact value for b because fast codes are available for the computation of gamma functions, a good approximation of b for $0.5 < n < 10$ is $2n - 1/3 + 0.009876/n$ (Prugniel & Simien 1997, see MacArthur, Courteau, & Holtzman 2003 for smaller values of n). Using the substitution $x = b(R/R_\mathrm{e})^{1/n}$, the total luminosity from equation (1) is given as

$$L_\mathrm{tot} = \int_0^\infty I(R') 2\pi R' \mathrm{d}R' = 2\pi I_0 R_\mathrm{e}^2 n b^{-2n} \Gamma(2n). \qquad (3)$$

For a sample of 250 dwarf elliptical and ordinary elliptical galaxies spanning $-13 > M_B > -23$ mag, Graham & Guzmán (2003) have shown how profile shape and surface brightness vary with galaxy magnitude. They found $M_B = -9.4 \log(n) - 14.3$, and $M_B = (2/3)\mu_0 - 29.5$ mag — until the presence of cores in galaxies brighter than ∼-20.5 B–mag. The latter phenomenon makes it more appropriate to use μ_e, the surface brightness at R_e, rather than the central surface brightness $\mu_0 = -2.5 \log(I_0)$. Doing so gives the expression $M_B = (2/3)(\mu_\mathrm{e} - 1.086b) - 29.5$ mag. Typical values are given Table 1.

A compendium of expressions related to Sérsic's $R^{1/n}$ model can be found in Graham & Driver (2005).

Table 1. Typical galaxy masses and central surface brightnesses $\mu_0 = -2.5\log(I_0)$ (using the inward extrapolation of the outer Sérsic profile in the case of "core" galaxies) associated with a range of Sérsic indices n. The mass estimates have come from the absolute B–band magnitudes in Graham & Guzmán (2003) using $M_{B,\odot}$=5.47 (Cox 2000) and M/L_B=5.31 (Worthey 1994, assuming a 12 Gyr population with Fe/H=0). The numbers are only indicative, with intrinsic variance playing a role amongst real galaxies.

Mass $M_\odot$	n	$\mu_{0,B}$ mag arcsec^{-2}
$\sim 10^7$	0.5	$\sim$27
$\sim 10^8$	1	$\sim$25
$\sim 10^9$	2	$\sim$20
$\sim 10^{11}$	4	$\sim$14
$\sim 10^{12}$	10	$\sim$9

2.1 Density

Generalising an expression from Mellier & Mathez (1987) that approximated the spatial, i.e. not projected, density profile of the $R^{1/4}$ model, Prugniel & Simien (1997) provide an analytical approximation to the density profile of the $R^{1/n}$ model. Lima Neto, Gerbal & Márquez (1999) showed that this spherical model is accurate to better than 5% over the radial range 10^{-2}–$10^3 R_e$. An even more accurate approximation for both spherical *and* triaxial stellar systems with $R^{1/n}$ light–profiles was developed by Trujillo et al. (2002), with an accuracy better than 0.1%. However, although analytical, the latter expression is not particularly simple. Impressively, an exact solution to the deprojection of the $R^{1/n}$ model, which obviously includes the $R^{1/4}$ case, was given in terms of Meijer G functions by Mazure & Capelato (2002); but again these equations are somewhat complicated[1]. Moreover, although these models can properly treat the range of outer profile shapes observed in real galaxies, they can not additionally allow for the presence of partially depleted cores. In fact, we are unaware of any density model capable of simultaneously describing the range of structure observed in both the inner and outer regime of galaxies with "cores".

The 3–parameter (ρ_0, R_e, n) density profile of Prugniel & Simien (1997; their equation B6) is relatively simple and can be written as

$$\begin{aligned} \rho(r) &= \rho_0 \left(\frac{r}{R_e}\right)^{-p} e^{-b(r/R_e)^{1/n}} \\ \rho_0 &= \frac{M}{L}\, I_0\, b^{n(1-p)}\, \frac{\Gamma(2n)}{2R_e\Gamma(n(3-p))}, \end{aligned} \tag{4}$$

where r is the spatial radius and ρ_0 is the normalisation such that the total mass from equation (4, see Appendix A) equals that from equation (1). We adopt Lima Neto et al.'s (1999) estimate, or rather the updated value given in Márquez et al. (2000), for the term p, for which a high–quality match between the exact, deprojected Sérsic profiles (solved numerically) and the above expression is obtained when $p = 1.0 - 0.6097/n + 0.05563/n^2$, for $0.6 < n < 10$ and $10^{-2} \le R/R_e \le 10^3$. The quantity $M/L \equiv \Upsilon$ is the mass–to–luminosity ratio, which is typically taken not to depend on galaxy radius but may of course do so. The density at $r = R_e$ is simply $\rho_0 e^{-b}$. Figure (2) shows the behaviour of this density profile for different values of profile shape n. Expressions and figures for the (enclosed) mass profile, the circular velocity, and the spatial and line–of–sight velocity dispersion are given in Appendix A for the spherical case.

Adding an inner power–law with slope γ, which is not to be confused with the incomplete gamma function $\gamma(a, x)$, we obtain the new model

[1] Exact analytical expressions for the mass, gravitational potential, total energy and the central velocity dispersion are also presented in Mazure & Capelato (2002). Exact numerical expressions are given in Ciotti (1991).

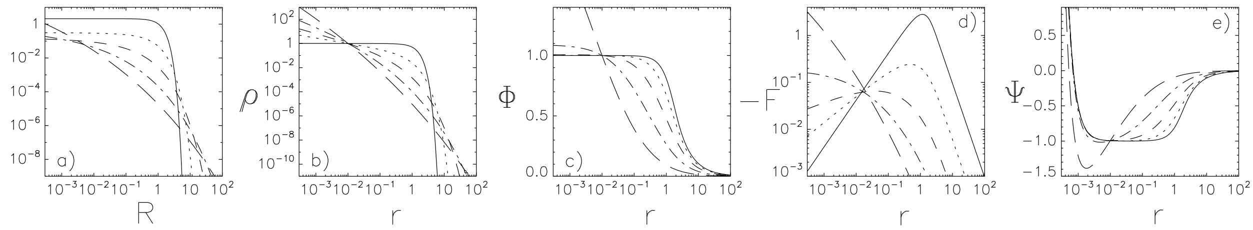

Figure 2. Core–less galaxies. Panel a) projected intensity I (exact numerical solution); panel c) potential (equation 8 divided by $\Phi(0.01R_{\rm e})$); panel d) force (equation 14); and panel e) pseudo potential (equation 15 divided by $|\Phi(0.01R_{\rm e})|$ with $h^2 = 10^{-6}|\Phi(0.01R_{\rm e})|$) associated with the Prugniel–Simien density profiles (equation 4) shown in panel b) for varying values of the profile shape n: $n = 0.5$ (solid lines), $n = 1$ (dotted), $n = 2$ (dashed), $n = 4$ (dash–dot), $n = 10$ (double–dash). The radius and density are normalised such that $R_{\rm e} = 1$ and $\rho(0.01R_{\rm e}) = 1$.

$$\begin{aligned}\rho(r) &= \rho' \left[1 + \left(\tfrac{r_b}{r}\right)^{\alpha}\right]^{\gamma/\alpha} \left\{\left[(r^{\alpha} + {r_b}^{\alpha})/{R_{\rm e}}^{\alpha}\right]^{-p/\alpha} {\rm e}^{-b\left[(r^{\alpha}+r_b^{\alpha})/R_{\rm e}^{\alpha}\right]^{1/n\alpha}}\right\} \\ \rho' &= \rho_b\, 2^{(p-\gamma)/\alpha} \left(\tfrac{r_b}{R_{\rm e}}\right)^{p} {\rm e}^{b\left(2^{1/\alpha} r_b/R_{\rm e}\right)^{1/n}}.\end{aligned} \tag{5}$$

The break radius, r_b, denotes the transition where the profile changes from one regime to the other, with ρ_b the density at this radius. The parameter α controls the sharpness of the transition. For $r << r_b$ equation (5) tends to a power–law with slope γ. For $r >> r_b$ equation (5) reduces to equation (4).

Modelling the light–profiles of luminous elliptical galaxies, Trujillo et al. (2004) have shown that the transition from the inner "core" to the outer Sérsic profile is probably rather sharp. Motivated by this result, we have chosen to make the transition between the inner power–law and the outer profile sharp by considering the $\alpha \rightarrow \infty$ limit. This reduces the above expression to a 5–parameter model capable of describing the entire radial extent of spherical stellar systems with power–law "cores", and can be written as

$$\begin{aligned}\rho(r) &= \rho_b \left[\left(\tfrac{r_b}{r}\right)^{\gamma} h(r_b - r) + \bar{\rho}\left(\tfrac{r}{R_{\rm e}}\right)^{-p} {\rm e}^{-b(r/R_{\rm e})^{1/n}} h(r - r_b)\right] \\ \bar{\rho} &= \left(\tfrac{r_b}{R_{\rm e}}\right)^{p} {\rm e}^{b(r_b/R_{\rm e})^{1/n}},\end{aligned} \tag{6}$$

where $h(x)$ is the Heaviside step function such that h=1 if $x > 0$ and h=0 if $x \leq 0$.

These spherical models are illustrated in Fig.3 e–h). In each panel a range of values of n has been used, while the value of γ increases sequentially from 0 to 1, 1.5 and finally 2. Depending on the parameter combination, one may have either a partially depleted core or a central excess — possibly representative of a nuclear star cluster or adiabatic growth around a supermassive black hole (e.g., Merritt 2004, and references therein). The break radius has been set to $0.01R_{\rm e}$, which a) matches the observed core–radii values of 0.01 to $0.02R_{\rm e}$ found by Trujillo et al. (2004, their table 2), and b) only uses the density profile from Prugniel & Simien (1997) over the radial range where it provides a high–quality match to a deprojected Sérsic profile. For reference, the nuclear star cluster "half–width at half–maximum" ($HWHM$) values divided by their host bulge $R_{\rm e}$ values in nucleated dwarf elliptical galaxies is 0.02 to 0.04 (Graham & Guzmán 2003, their table 2).

2.2 Gravitational Potential and Force

We derive an expression for the potential (assuming spherical symmetry) using the inverted form of the Poisson equation (e.g., Binney & Tremaine 1987, their equation 2-22):

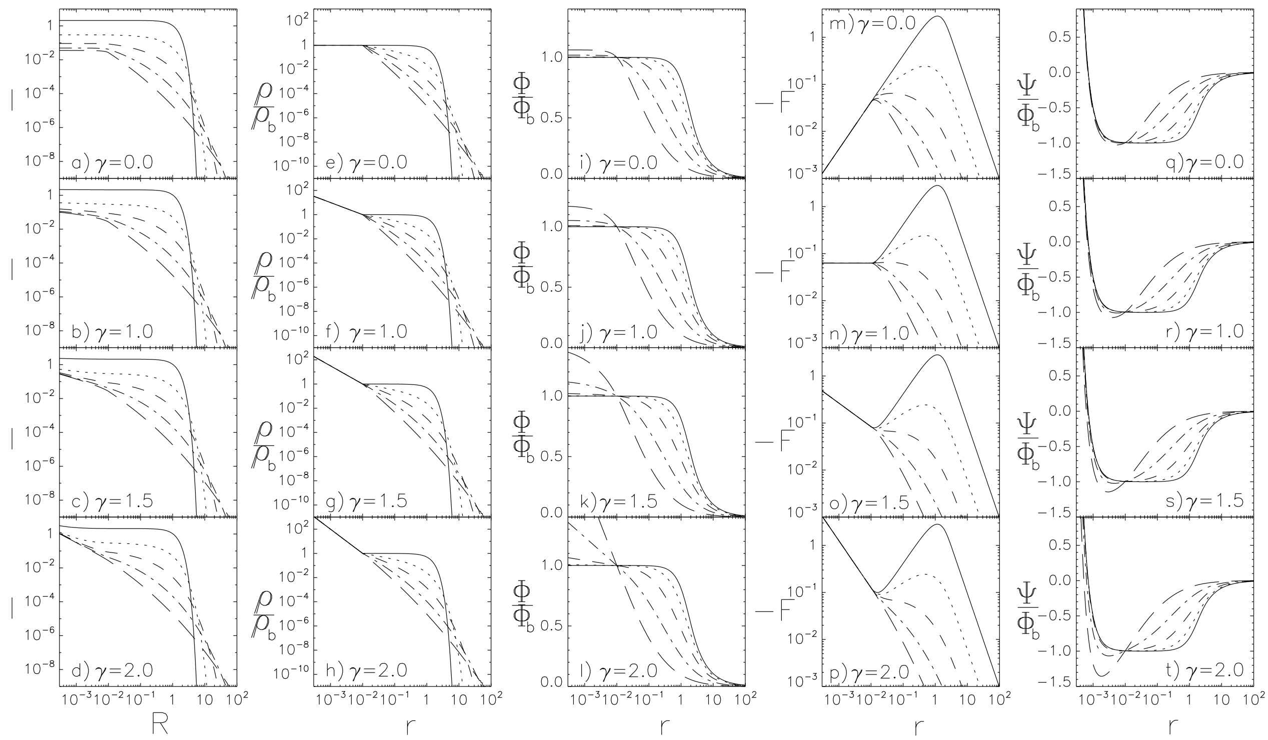

Figure 3. Core galaxies. Panels a–d) show the projected intensity I (equation 18, exact numerical solution); panels i–l) show the potential (equation 8 divided by $\Phi(r = r_b)$); panels m–l) show the force (equation 14); and panels q–t) show the pseudo potential (equation 15 divided by $|\Phi(r = r_b)|$ with $h^2 = 10^{-6}|\Phi(r = r_b)|$) associated with the density profiles (equation 6) in panels e–h), for varying values of the outer profile shape n: $n = 0.5$ (solid lines), $n = 1$ (dotted), $n = 2$ (dashed), $n = 4$ (dash-dot), $n = 10$ (double–dash); and varying central cusp slope γ. In these figures the scale radius R_e has a value of 1, as does the scale density ρ_b which occurs at a radius $r_b = 0.01R_e$.

$$\Phi(r) = -4\pi G\left[\frac{1}{r}\int_0^r \rho(\bar{r})\bar{r}^2 d\bar{r} + \int_r^\infty \rho(\bar{r})\bar{r} d\bar{r}\right]. \tag{7}$$

After some algebraic manipulation (see Appendix B), one obtains

$$\Phi(r) = -4\pi G \left\{ \begin{array}{ll} \frac{1}{r}J_1(r) + J_2(r) + L_1(r_b) & \text{if } r \le r_b, \\ \frac{1}{r}J_1(r_b) + \frac{1}{r}L_2(r) + L_1(r) & \text{if } r > r_b, \end{array} \right. , \tag{8}$$

where

$$J_1(r) = \rho_b {r_b}^\gamma r^{3-\gamma}/(3-\gamma) \qquad \text{if } \gamma < 3 \tag{9}$$

$$J_2(r) = \rho_b {r_b}^\gamma \left\{ \begin{array}{ll} \frac{1}{2-\gamma}\left({r_b}^{2-\gamma} - r^{2-\gamma}\right) & \text{if } \gamma \ne 2 \\ \ln\frac{r_b}{r} & \text{if } \gamma = 2 \end{array} \right. , \tag{10}$$

$$L_1(r) = \rho_b \bar{\rho} {R_e}^2 n b^{n(p-2)} \Gamma\left(n(2-p), b\left(\frac{r}{R_e}\right)^{1/n}\right), \tag{11}$$

$$L_2(r) = \rho_b \bar{\rho} {R_e}^3 n b^{n(p-3)} \left[\Gamma\left(n(3-p), b\left(\frac{r_b}{R_e}\right)^{1/n}\right) - \Gamma\left(n(3-p), b\left(\frac{r}{R_e}\right)^{1/n}\right)\right], \tag{12}$$

and

$$\Gamma(a,x) = \int_x^\infty e^{-t} t^{a-1} dt, \quad a > 0 \tag{13}$$

is the complement to the incomplete gamma function shown in equation (2). Although J_1 diverges when $\gamma = 3$, this is unlikely to be a problem because such steep inner profile slopes are not observed in real galaxies (e.g. Gebhardt et al. 1996; Milosavljević et al. 2002; Ravindranath, Ho, & Filippenko 2002). Fig.3i–3l show the gravitational potential of this model as a function of spatial radius r. The case when the break radius equals zero is shown in Fig. (2c).

The central potential $\Phi(0) = -4\pi G[J_2(0) + L_1(r_b)]$, for $\gamma \neq 2$. When $r_b = 0$, $\Phi(0) = -4\pi G L_1(0)$, with $\rho_b \bar{\rho} = \rho_0$.

The corresponding radial force is computed by differentiation with respect to the spatial radial coordinate r. After some algebraic cancellations (see Appendix B), the force is found to be

$$F(r) = -\frac{d\Phi}{dr} = 4\pi G \begin{cases} -\frac{1}{r^2} J_1(r) & \text{if } r \leq r_b, \\ -\frac{1}{r^2} J_1(r_b) - \frac{1}{r^2} L_2(r) & \text{if } r > r_b, \end{cases} . \tag{14}$$

We remind readers of the logarithmic radial scale used in Fig. 3, and caution that the gradient to the curves shown in Fig.3i–3l should be interpreted with care when comparing them with the force shown in Fig.3m–3p. The case when the break radius equals zero is shown in Fig. (2d).

In order to carry out orbital integration, one needs to compute the force along an orbit. For a fixed break radius r_b, the term in the first half of the expression $L_2(r)$ is constant and therefore only needs to be computed once at the beginning of a simulation. Therefore, the incomplete gamma function $\Gamma(a, x)$ need only be called once per evaluation of the force (the term in the second half of $L_2(r)$), and not at all if the star is inside the break radius, i.e. $r < r_b$.

The abrupt change in the force — whose nature is not only dependent on the value of the inner profile slope γ and the Sérsic index n but also on the ratio r_b/R_e — is not a problem for constructing models because the force remains both negative and continuous at r_b. Orbit stability can be checked using the "pseudo" potential $\Psi(r)$, sometimes also referred to as the "effective" potential (Landau & Lifshitz 1976; Goldstein 1980), and given by

$$\Psi(r) = \Phi(r) + \frac{h^2}{2r^2}, \tag{15}$$

where h is the angular momentum per unit mass. Uisng $h^2 = 10^{-6}|\Phi(0.01R_\mathrm{e})|$, and normalising $\Psi(r)$ by dividing by $|\Phi(0.01R_\mathrm{e})|$, in order to highlight orbits near the radius $0.01R_\mathrm{e}$, Fig.3q–3t reveals that the abrupt change in density and force at r_b does not result in a double minimum for the pseudo potential — which would be indicative of an unstable configuration. Instead, for a given orbital energy less than zero, particles remain bound within the curve defined by the pseudo potential.

In summary, we have a set of equations consisting of analytical expressions, and one special function for which fast computer codes exist, that can a) simulate the range of observed light–profile shapes and b) model partially depleted cores and/or certain additional nuclear components.

2.3 Projected Surface Brightness Profile

The projection of the above density profile, i.e. the intensity–profile or "light–profile", is computed by solving the Abel integral

$$I(R) = \frac{2}{\Upsilon} \int_R^\infty \frac{\rho(r) r}{\sqrt{r^2 - R^2}} dr, \tag{16}$$

where R is the projected radius and Υ is the mass–to–luminosity ratio. If equation (6) is rewritten as $\rho(r) = \rho_1(r) + \rho_2(r)$, where

$$\begin{aligned}\rho_1(r) &= \rho_b \left(\frac{r_b}{r}\right)^{\gamma} h(r_b - r), \quad \text{and} \\ \rho_2(r) &= \rho_b \bar{\rho} \left(\frac{r}{R_{\rm e}}\right)^{-p} {\rm e}^{-b(r/R_{\rm e})^{1/n}} h(r - r_b),\end{aligned} \tag{17}$$

then the corresponding intensity can be expressed as

$$I(R) = \begin{cases} \frac{2}{\Upsilon}\int\limits_R^{r_b} \frac{\rho_1(r)r}{\sqrt{r^2-R^2}}dr + \frac{2}{\Upsilon}\int\limits_{r_b}^{\infty} \frac{\rho_2(r)r}{\sqrt{r^2-R^2}}dr \equiv I_1(R) + I_2(R; r_b) & \text{if } R \le r_b, \\ \frac{2}{\Upsilon}\int\limits_R^{\infty} \frac{\rho_2(r)r}{\sqrt{r^2-R^2}}dr \equiv I_2(R) & \text{if } R > r_b. \end{cases} \tag{18}$$

As shown in Appendix B, the first term $I_1(R)$ is such that

$$I_1(R) = \frac{2}{\Upsilon}\rho_b {r_b}^{\gamma} \begin{cases} \sqrt{r_b^2 - R^2} & \text{if } \gamma = 0, \\ \ln \frac{r_b + \sqrt{r_b^2 - R^2}}{R} & \text{if } \gamma = 1, \\ R^{-1} \sin^{-1} \sqrt{1 - R^2/r_b^2} & \text{if } \gamma = 2, \\ \frac{1}{2} R^{1-\gamma} B_{1-R^2/{r_b}^2}\left(\frac{1}{2}, \frac{\gamma-1}{2}\right) & \text{otherwise,} \end{cases} \tag{19}$$

with B the incomplete Beta function defined as

$$B_x(y,z) = \int\limits_0^x u^{y-1}(1-u)^{z-1}du. \tag{20}$$

The only expressions we do not provide an exact equation for are $I_2(R)$ and $I_2(R; r_b)$. However, because Prugniel & Simien (1997) devised equation (4) to match the deprojected form of the Sérsic light–profile, it makes sense to use the $R^{1/n}$ model as a suitable approximation. One therefore has that

$$I_2(R) \approx I_{\rm e} {\rm e}^{b} {\rm e}^{-b(R/R_{\rm e})^{1/n}} \tag{21}$$

with $I_{\rm e}$ the (projected) intensity at the (projected) radius $R_{\rm e}$. The value of $I_{\rm e}$ can be set in terms of the density model parameters if one applies the condition that the total mass given by equation (21, see equation 3) equals the total mass from equation (4, see Appendix A), yielding

$$I_{\rm e} = \frac{2{\rm e}^{-b} R_{\rm e} \rho_b \bar{\rho} \Gamma(n(3-p))}{\Upsilon \Gamma(2n) b^{n(1-p)}}, \tag{22}$$

with $\bar{\rho}$ given in equation (6). Over the radial interval $10^{-2} \le R/R_{\rm e} \le 10^2$, the maximum difference in surface brightness between this approximation for $I_2(R)$ and the exact value is about 0.1 mag arcsec^{-2} if $n > 2$, and only 0.04 mag arcsec^{-2} when $n = 4$ (Fig. 4). For a Gaussian profile ($n = 0.5$) the agreement is very good, while for an exponential profile ($n = 1$) the match at large radii is rather poor — increasing to $\sim$0.2 mag arcsec^{-2} at $R/R_{\rm e} = 100$.

The only term requiring numerical evaluation is $I_2(R; r_b)$, although, if desired, one may choose to additionally evaluate $I_2(R)$ numerically rather than using the analytical approximation given in equation (21). Given that the intensity profile is likely only computed at the end, or at a few intermediate stages, of a simulation, the computation time involved in deriving the light–profile is not a concern.

The exact (numerically computed) projected light–profiles associated with the density models in Fig. (2b) are shown in Fig. (2a), and those in Fig.3e–3h are shown in Fig.3a–3d.

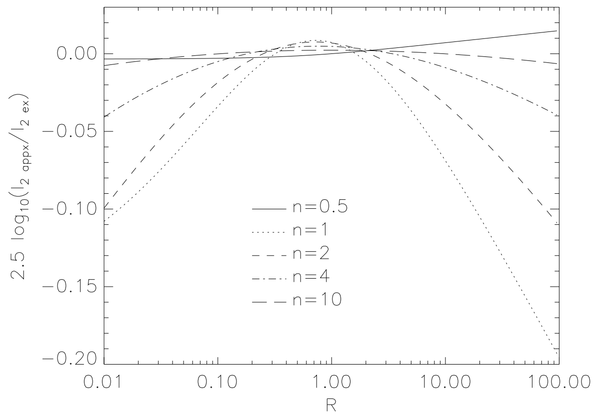

Figure 4. The relative error between the term $I_2(R)$ given in equation (18) and the approximation given in equation (21) is shown as a function of radius, normalised by the effective radius $R_{\rm e}$, for varying light–profile shapes n.

In passing we note that when $\gamma = 0$ and $R < r_b$, the slope of the surface brightness profile is close to but not exactly zero (Fig.3a). We also note that the value of $I_{\rm e}$ and $R_{\rm e}$ are stable against increases in r_b and changes in γ because they pertain to the outer, undisturbed profile when there is a partially depleted core, and to the underlying host galaxy profile when a central flux excess is present. As such, when $r_b > 0$, $I_{\rm e}$ and $R_{\rm e}$ are not the total galaxy half–light values. In practice, the stellar flux deficit is only $\sim$0.1% for "core" galaxies (Graham 2004) and the stellar flux excess $\sim$1% in nucleated dwarf elliptical galaxies (Graham & Guzmán 2003), and so the actual discrepancy is not greater than $\sim$1%.

3 APPLICATION TO REAL GALAXY PROFILES

Over a quarter of a century ago, de Vaucouleurs & Capaccioli (1979) demonstrated that, when the inner 10 arcseconds were excluded, the $R^{1/4}$ model provided a very good fit to the light–profile of NGC 3379 ($M_B \sim -20$ mag). Since then, Capaccioli and his collaborators have shown that different galaxies can be equally well fit, but only by using models with a very different curvature (e.g., Caon et al. 1993). Bertin, Ciotti & Del Principe (2002) have shown $R^{1/n}$ fits to the circularised light–profiles of four (illustrative) galaxies from Caon et al. (1993). Here we deproject these galaxies' major–axis light–profiles and fit the Jaffe, Hernquist and Dehnen models, and explore how well they describe the luminosity–density profile in comparison with the model of Prugniel & Simien (1997) given in equation (4). In addition, we include the *HST*–resolved dwarf elliptical galaxy[2] LGC 47 (Stiavelli et al. 2001), and the "core" galaxy NGC 3348 (Rest et al. 2001; Trujillo et al. 2004) to which we apply our new core-density model (equation 6).

3.1 Sérsic and core–Sérsic model

Fig.5 shows the Sérsic (1963, 1968) model applied to the ground–based, major–axis, B–band light–profiles of NGC 1379, 4458, 4374, and 4552, and applied to the *HST*–based, major–axis, I–band light–profile of LGC 47. The data have come from Caon et al. (1993) and Stiavelli et al. (2001), respectively. Also shown is the core–Sérsic model (Graham et al. 2003b; Trujillo et al. 2004) applied to the *HST*–based, major–axis, R–band light–profile of

[2] LGC: Leo Group Catalog.

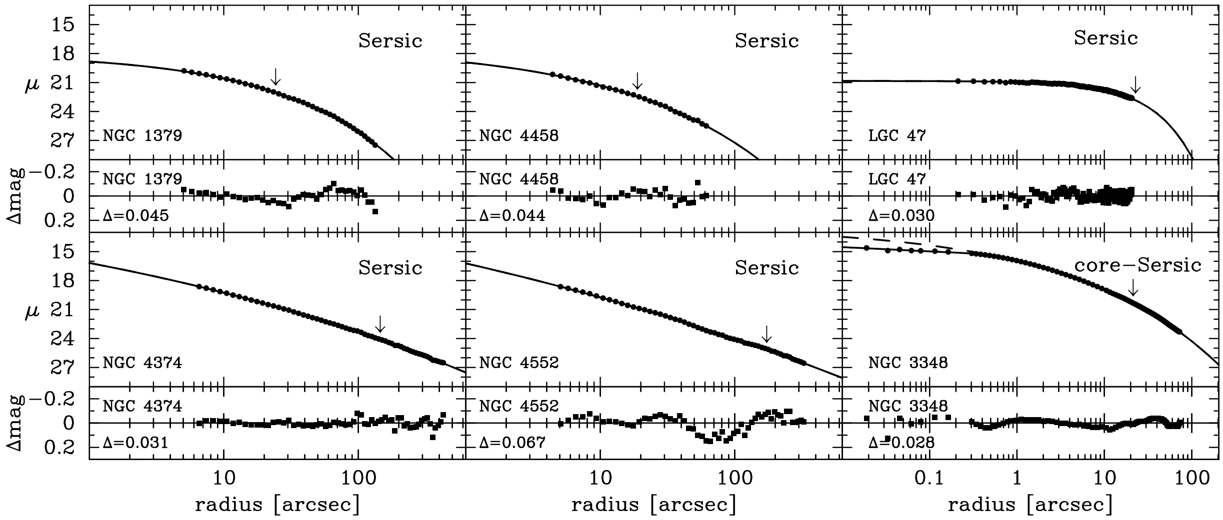

Figure 5. Best–fitting Sérsic model to the major–axis, B–band light–profiles of NGC 1379, 4458, 4374 and 4552 (data from Caon et al. 1990; Caon et al. 1993), and the major–axis, I–band light–profile of LGC 47 (data from Stiavelli et al. 2001). The best–fitting core–Sérsic model to the major–axis, R–band light–profile of the "core" galaxy NGC 3348 is also shown (data from Trujillo et al. 2004); the inward extrapolation of the outer Sérsic profile is shown by the dashed curve. The model parameters are given in Table 2. The effective half–light radii are marked with an arrow.

Table 2. Sérsic and core–Sérsic parameters from the fits in Fig.5.

Gal Id.	Dist. mod.	Band	μ_e mag arcsec^{-2}	R_e $''$	n	γ	R_b $''$	μ_b mag arcsec^{-2}
NGC 1379	31.51	B	22.02	24.3	2.0	...	...	...
NGC 4458	31.18	B	22.46	18.9	2.6	...	...	...
LGC 47	30.30	I	22.84	22.7	1.1	...	...	...
NGC 4374	31.32	B	24.11	146	8.2	...	...	...
NGC 4552	30.93	B	25.16	172	11.8	...	...	...
NGC 3348	33.08	R	...	21.4	3.8	0.18	0.43	15.30
NGC 2986	32.31	R	...	75.7	6.7	0.25	0.77	15.60
NGC 4291	32.09	R	...	17.8	5.3	0.14	0.38	14.54

NGC 3348. Table 2 shows the best–fitting parameters. For the first four galaxies, the values agree with those reported in Caon et al. (1993), with the exception that we find a slightly smaller value of n for NGC 4552. However, the difference between an $n = 12$ and $n = 14$ profile is minimal. For LGC 47, Stiavelli et al. (2001) presented fits to the geometric mean ($r = \sqrt{ab}$), V–band light–profile, finding $n \sim 1.5$. Due to possible colour gradients, and ellipticity gradients, it is expected that our fit to the major–axis, I–band light–profile may be slightly different: nonetheless, we derived a similarly small value of $n = 1.1$. NGC 1379 and NGC 4458 have values of $n = 2.0$ and 2.6 respectively. NGC 4374 and NGC 4552 have values of ~ 8 and ~ 12, considerably greater than 4. On the other hand, NGC 3348 has a value of n close to 4, but possesses a distinct core. Although it is likely the large galaxies NGC 4374 and NGC 4552 may also possess a partially depleted core, the inner few arcseconds have been excluded from their profile due the effects of seeing.

3.2 Density profiles

In order to obtain each galaxy's deprojected light–profile, a non–parametric deprojection was used when solving the appropriate Abel integral. The best–fitting light–profile models were however used to extrapolate the observed light–profiles to infinity. This simply meant using the best-fitting Sérsic model to extend the observed data to larger radii in order for one to compute the deprojected light–profile, i.e. the density profile. The actual choice of extrapolation only affects the outer luminosity–density profile slightly. Due to the coarser radial sampling of the ground–based profiles than the *HST* profiles, their deprojected profiles are somewhat noisier. We applied box–cart smoothing with four different box sizes and refitted the various density models; in every instance the best–fitting model parameters where practically identical, suggesting such noise is not an issue.

In the case of the dwarf elliptical galaxy LGC 47, its observed (exponential) light–profile only went out to 1 $R_{\rm e}$, not enough to properly show how such stellar distributions decline at large radii. For this galaxy only, we model the density profile to radii larger than observed. Given that galaxies, and bulges, with exponential profiles do exist, we felt that the analysis of such a profile would be of value.

The luminosity–density profiles (Fig.6–10) have been calibrated in units of $L_\odot$ pc^{-3} using the distance moduli provided in Tonry et al. (2001) for the Caon et al. sample, and a distance of 41 Mpc for NGC 3348 and 11.5 Mpc for LGC 47, taken from their respective papers. We used solar absolute magnitudes of M_B=5.47, M_R=4.28 and M_I=3.94 (Cox 2000). A Hubble constant $H_0 = 75$ km s^{-1} Mpc^{-1} was used.

The value of Δ associated with the residual profiles shown in Fig.6–10 is not quite the rms error, but is computed using the expression

$$\Delta = \frac{\sqrt{\sum_{i=1}^{m} {\delta_i}^2}}{m-k}, \tag{23}$$

where m is the number of data points, δ_i is the i th residual and k is the number of parameters in the fitted model. Because the different models have different numbers of free parameters, this provides a more appropriate measure for model comparison.

3.3 Jaffe model

Fig.6 presents the best–fitting (2–parameter) Jaffe (1980) model, $\rho(r) = [4\rho(a)](r/a)^{-2}(1 + r/a)^{-2}$, to each galaxy's luminosity–density profile. The scale–length is denoted by a, and $\rho(a)$ is simply the density at $r = a$. The position of the transition radius, i.e. the scale–length, where this model changes from an inner power–law slope of -2 to an outer power–law slope of -4 is marked with an arrow in Fig.6. In the case of LGC 47 and NGC 3348, the Jaffe model is clearly inadequate to describe the stellar profile. We also note that the best–fitting models have transition radii well beyond the observed radial extent of the galaxies. The hump–shaped residual profiles (upper panels) for the low n galaxies NGC 1379 and NGC 4458, and the bowl–shaped residual profiles for the high n galaxies NGC 4374 and NGC 4552 are clear indications that the Jaffe model is unable to match the global curvature in these galaxies' stellar distributions.

3.4 Hernquist model

In Fig.7 one can see the best–fitting (2–parameter) Hernquist (1990) models, $\rho(r) = [8\rho(a)](r/a)^{-1}(1+ r/a)^{-3}$. This model is also incapable of describing the core galaxy NGC 3348, and the hump/bowl shaped residual profiles of the other galaxies largely reflects the failure seen with the Jaffe model. We do however note that in the case of NGC 4458, the (non-core) galaxy with the closest Sérsic index to a value of 4, the fit is quite acceptable.

3.5 Dehnen model

The (3–parameter) Dehnen (1993) model, $\rho(r) = [2^{4-\gamma}\rho(a)](r/a)^{-\gamma}(1 + r/a)^{\gamma-4}$, which subsumes the first two models as special cases, does noticeably better. This is due to the fact

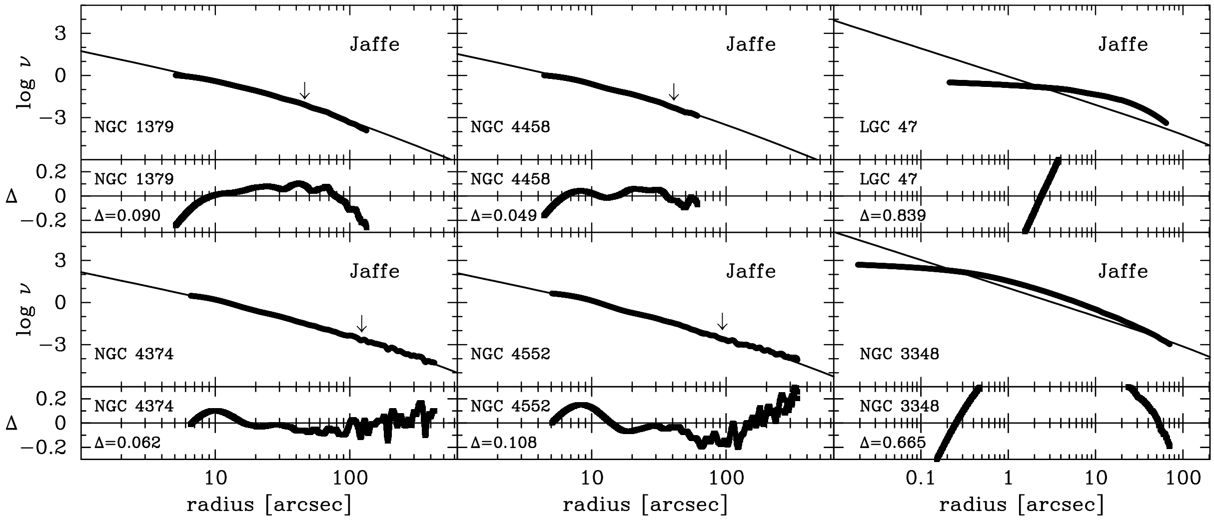

Figure 6. Best–fitting Jaffe model to the deprojected light–profiles of the galaxies in Fig.5. The luminosity–density profile $\nu(r) = \rho(r)/(M/L)$ is in units of $L_{\odot,B}$ pc^{-3} for NGC 1379, 4458, 4374 and 4552, $L_{\odot,R}$ pc^{-3} for NGC 3348, and $L_{\odot,I}$ pc^{-3} for LGC 47. The model parameters are given in Table 3. The arrow denotes the size of the scale radius a.

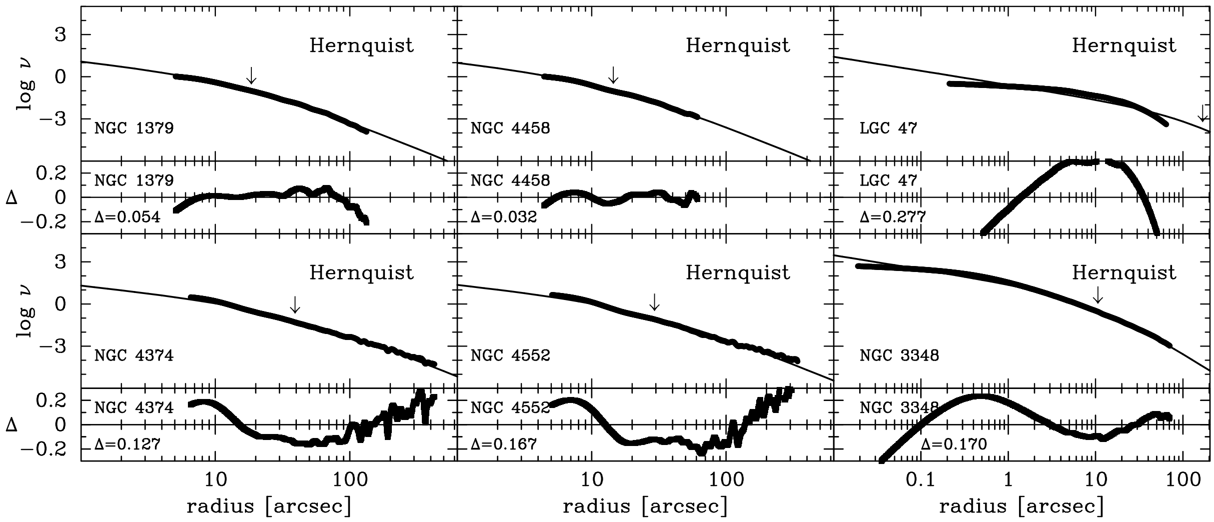

Figure 7. Same as Fig.6, except that the best–fitting Hernquist models are shown.

that it has an additional (third) parameter over the previous two models that actually measures the inner power–law slope, rather than assuming some fixed value. Obviously the Dehnen model fails to fit the detailed profile of NGC 3348. In a sense, it also fails to match NGC 4552, setting the transition radius to 500″ — an arbitrary large upper limit in our code — well outside of the observed radial range. The reason for this large transition radius is however understood. Graham & Driver (2005) show that for large values of n, the Sérsic model tends to a power–law such that $I(R) \sim R^{-2}$; which results in $\rho(r) \sim r^{-3}$. NGC 4552 has the largest value of n in our sample, and the optimal Dehnen model is simply a (single) power–law with slope γ.

In the case of the lower n galaxies (LGC 47 and NGC 1379), one can see that the Dehnen model — constructed to match $R^{1/4}$ light–profiles — does not decline as quickly as the observed structures. Due to the fact that we used an exponential–like model (n=1.1) to extrapolate the light–profile of LGC 47, this eliminates the possibility that the observed mismatch at large radii may be unique to this galaxy. Rather, the mismatch reflects the

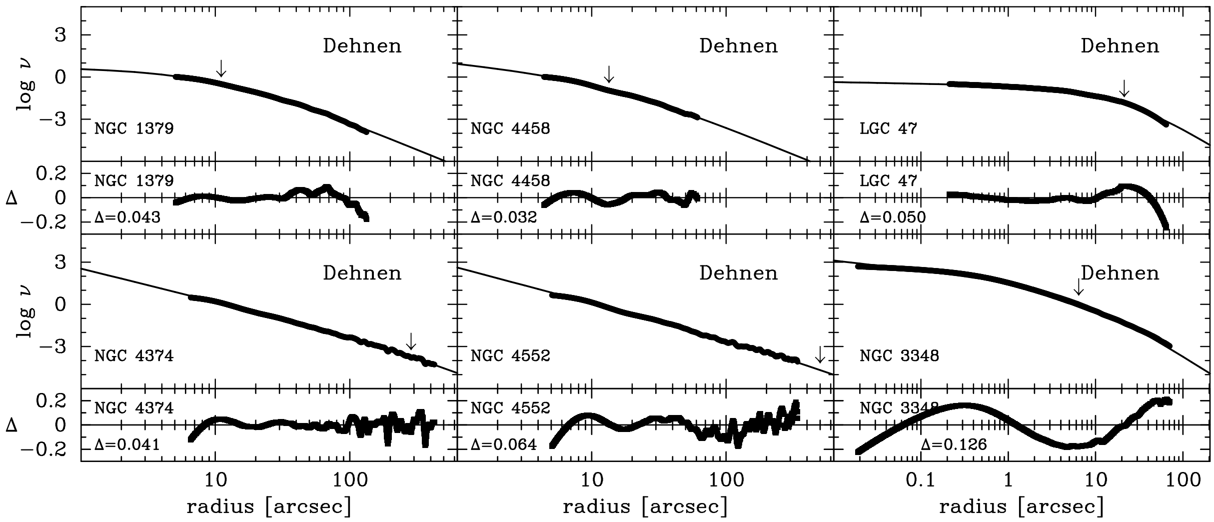

Figure 8. Same as Fig.6, except that the best–fitting Dehnen models are shown.

Table 3. Best–fitting parameters from a range of density models. The units are $L_{\odot}$ pc^{-3} for ρ and arcseconds for a.

Gal.	Band	Jaffe		Hernquist		Dehnen			Equation (6)					
Id.		a	$\log\rho(a)$	a	$\log\rho(a)$	a	$\log\rho(a)$	γ	R_e	$\log\rho(R_e)$	n	γ	r_b	$\log\rho(r_b)$
NGC 1379	B	46.2	-2.17	18.5	-1.03	11.1	-0.49	0.00	24.7	-1.31	2.1	...	...	...
NGC 4458	B	40.8	-2.27	14.5	-0.99	13.5	-0.91	0.89	18.8	-1.28	2.5	...	...	...
LGC 47	I	500	-6.07	168	-3.71	21.3	-1.91	0.12	22.4	-1.85	0.9	...	...	...
NGC 4374	B	123	-2.61	39.2	-1.16	285	-3.74	2.36	131	-2.73	7.7	...	...	...
NGC 4552	B	93.9	-2.45	29.3	-0.97	500	-4.68	2.54	168	-3.21	10.8	...	...	...
NGC 3348	R	500	-4.97	10.6	0.46	06.4	0.14	0.71	20.2	...	3.6	0.44	0.37	2.15
NGC 2986	R	...	...	...	...	...	...	...	79.1	...	6.5	0.71	0.78	1.92
NGC 4291	R	...	...	...	...	...	...	...	21.4	...	5.6	0.43	0.46	2.56

well known fact that exponential light–profiles have outer density profiles that decline more quickly with radius than r^{-4}. Not surprisingly, an almost identical result to that seen in Fig. 8 for LGC 47 is obtained when we deproject a pure $n = 1$ exponential light–profile. As a rule, the lower the value of the Sérsic index n, the steeper the outer decline in density and the greater the mismatch with the Dehnen model.

3.6 Prugniel–Simien density profile, and our adaptation for galaxies with power–law cores

Fig.9 presents the best–fitting (3–parameter) model of Prugniel & Simien (1997). Aside from NGC 3348, the fits are obviously rather good, with only NGC 4552 suggesting the presence of additional fine structure that has been missed. In fact, Caon et al. (1993) classified this as a lenticular galaxy; the other galaxies are elliptical, i.e. they do not have an embedded large–scale disk. With the exception of the core galaxy NGC 3348, every fit is equal to or better than those obtained with the (3–parameter) Dehnen model. This is especially the case for the low n galaxies LGC 47 and NGC 1379.

Fig.10 presents the new (5–parameter) model (equation 6) applied to the core galaxy NGC 3348. The model performs well and is the only density model we are aware of that can fit galaxies possessing partially depleted cores. The best–fitting parameters are given in Table 3. Although the luminosity–density at a spatial radius r equal to R_e is not a formal parameter of the new model, it is equal to $10^{-1.26} L_{\odot,R}$ pc^{-3} for NGC 3348.

We have also included two additional "core" galaxies: NGC 2986 and NGC 4291. The best–fitting core-Sérsic parameters derived here for NGC 4291 are the same as those given in

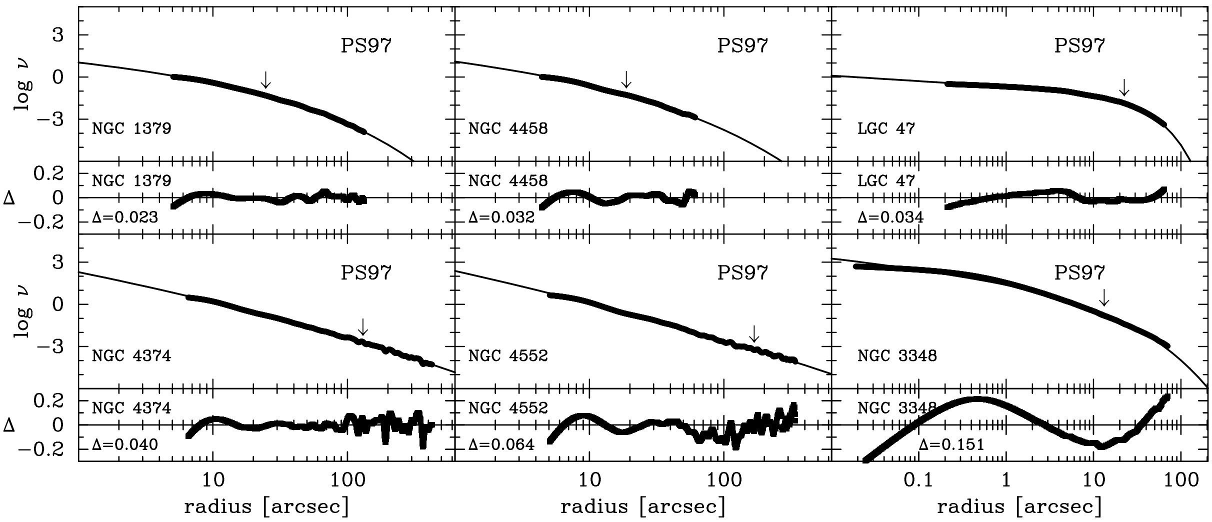

Figure 9. Same as Fig.6, except that the best–fitting model of Prugniel & Simien (1997), as given by equation (4), is shown here. The arrow marks the radius $R_{\rm e}$.

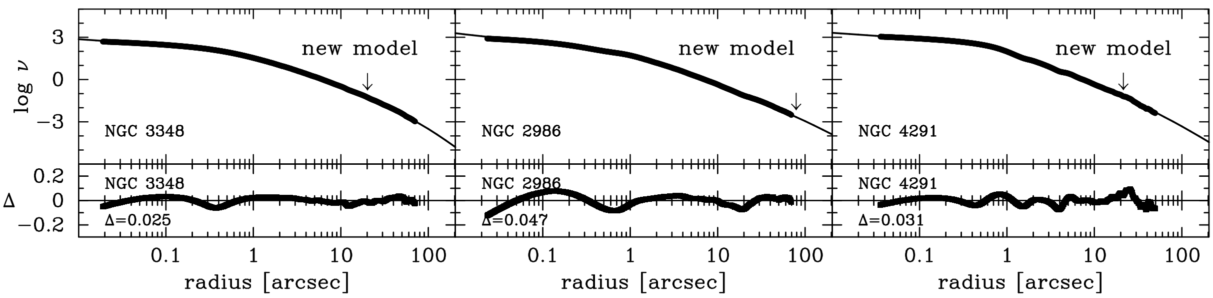

Figure 10. New density model (equation 6) applied to the core galaxies NGC 3348, 2986 and 4291. The arrow marks the model radius $R_{\rm e}$.

Trujillo et al. (2004), as was the case with NGC 3348. However, our core–Sérsic parameters for NGC 2986 are somewhat different; the reason is due to the fact that we exclude the (highly deviant) outermost two data points from the light–profile given in Trujillo et al., which may be due to poor sky–subtraction. Although the core–parameters did not change much, the value of n increased by 25% and R_e increased from 44 to 76 arcseconds.

NGC 2986 and NGC 4291 were not shown in the previous figures because they had residual profiles very similar to that seen for NGC 3348. They are included here so one can see the new model's applicability to other core galaxies. Interestingly, the residual profiles seem to suggest that the core density profiles have only approximately a power–law structure.

4 DISCUSSION

Just like the $R^{1/4}$ model, the $R^{1/n}$ model was offered as an empirical fitting function. A physical basis for its origin is not widely recognised. Márquez et al. (2000, 2001, and references therein) have argued it is a natural result from the (near) conservation of specific entropy. Other theoretically motivated models, based on the statistical mechanics of partially complete violent relaxation, also lead to density profiles that match deprojected Sérsic $R^{1/n}$ profiles, at least for $2.5 < n < 8.5$ (Trenti & Bertin 2005, see also Hjorth & Madsen 1995). We do not, however, attempt to solve this question here, but do note that the

Jaffe, Hernquist and Dehnen models, like the new model presented here, are simply useful empirical fitting functions.

Fig.6 and 7 clearly reveal that the Jaffe and Hernquist models fail to describe the stellar distribution of low– and high–n galaxies, relative to $n = 4$. This is not particularly surprising as they were only designed to match galaxies with an $n = 4$ light–profile. The Dehnen model does better, but fails to model the lower n galaxies in our sample. This can be seen in the outer part of the profile for NGC 1379 and LGC 47 in Fig. 8, where the density declines more rapidly with radius than r^{-4}. At the high–n end, the (projected) intensity profile $I(r) \to r^{-2}$ as the Sérsic index $n \to \infty$ (Graham & Driver 2005), and the density profile tends towards a power-law with $\rho(r) \to r^{-3}$. For reference, the isothermal model has $\rho(r) \propto r^{-2}$. Ignoring the presence of partially depleted cores, for galaxies with values of n greater than $\sim$8, a single power–law can approximate their density profiles and the Dehnen model appears to work well, albeit by setting the scale radius, a, to very large radii.

Zhao (1996) developed a 5–parameter generalisation of the Dehnen model such that both the inner and outer power–law slope can be adjusted, along with the radius, density and sharpness of the transition region. The model was first introduced by Hernquist (1990, his equation 43) and has the same structural form as the "Nuker" model (e.g., Lauer et al. 1995). However, as explained in Graham et al. (2002, 2003b), such double power–law models are not appropriate for describing profiles with obvious logarithmic curvature, that is, profiles without inner and outer power–laws but whose slopes continuously vary as a function of radius — which is the case for the luminosity–density profiles of most elliptical galaxies and bulges. Although in the absence of a partially depleted stellar core this model should be able to approximate real luminosity–density profiles, themselves are highly sensitive to the fitted radial range. This is because the parameters simply adjust themselves in order to match the curvature in whatever part of the profile one includes in the fit, providing inner and outer power–law slopes that are a product of the radial range sampled. Consequently, this model is not explored here. The 3–parameter model of Prugniel & Simien (1997) was, however, designed to describe profiles with curvature and does therefore not suffer from such a problem.

The density profile of Prugniel & Simien (equation 4) may prove helpful for describing gravitational lenses (e.g., Cardone 2004; Kawano et al. 2004) and the dark matter distributions of halos built in ΛCDM cosmological simulations. Demarco et al. (2003) have already observed the hot gas in galaxy clusters to have a (projected) Sérsic distribution. Intriguingly, the curved nature of simulated dark matter profiles has resulted in the recent discovery that Sérsic's model describes them better than the generalised NFW[3] double power–law model with inner and outer slopes of -1 and -3, respectively (Merritt et al. 2005). Whether or not they were aware of the fact, Navarro et al. (2004; their equation 5) and Cardone, Piedipalumbo & Tortora (2005; their equation 10) presented Sérsic's model as a leading candidate to describe the density profiles of dark matter halos. It would be of interest to investigate whether the generalisation of the Mellier–Mathez (1987) model presented by Prugniel & Simien (1997) (equation 4 in this paper) may be useful, if not even more appropriate, for such studies.

The new density–potential pair should also prove fruitful for simulations of bulges in disk galaxies. To date, such studies have usually been performed using models which are inappropriate for describing the majority of bulges. This situation has arisen from improved

[3] If cosmological simulations of dark matter halos indeed have density profiles which are logarithmically curved, i.e. if they have slopes which vary continuously with radius (e.g. Navarro et al. 2004; Hansen & Moore 2005), then the issue of whether the central cusp slope is -1 or -1.5 or smaller may need to be reconsidered.

observations which have shown bulges typically have Sérsic indices n ranging from 0.5 to 3, rather than 4 (e.g., Andredakis & Sanders 1994; de Jong 1996; Graham 2001; MacArthur et al. 2003).

It is hoped that the models presented here will additionally enable one to perform a number of simulations testing various observational results and theoretical problems associated with the influence of SMBHs on central density cusps and the connection with the global stellar structure. The influence of SMBHs on the stellar dynamics (e.g., Baes, Dejonghe & Buyle 2005) can also be explored as a function of various physical parameters. One way this can be achieved is by investigating the restrictions that self–consistency requirements pose on galaxy density profiles (e.g., Terzić 2003). Other numerical simulations may investigate the effects of binary SMBHs at the centers of galaxies (e.g., Graham 2004). Gravitational scattering (e.g., Makino & Funato 2004), as well as resonant chaotic phase mixing between the frequencies of the binary orbit and the natural frequencies of stellar orbits, can cause a significant redistribution of mass extending well beyond the radius of the binary (Kandrup et al. 2003; see also Merritt & Poon 2004). One could also address the similarities and differences between the nature and efficiency of chaotic phase mixing in the new model (both time–independent and subjected to time–periodic pulsations) and previous studies that have used somewhat more limited potentials (e.g., Kandrup & Mahon 1994, Merritt & Valluri 1996; Siopis & Kandrup 2000, Terzić & Kandrup 2004). In addition, one should be able to extend past work which has explored the evolution of galaxies using models that had a restricted range of outer galaxy structure (e.g., Merritt & Fridman 1996; Poon & Merritt 2002, 2004). Furthermore, it is hoped one will explore *new* connections between the outer galaxy structure, i.e. profile shape, and the properties of the core, such as the inner cusp slope, core size, and black hole mass.

5 SUMMARY

Our application of the (2–parameter) Jaffe and Hernquist models to a sample of luminosity–density profiles taken from real galaxies reveals that these models are inadequate for describing the observed range of stellar distributions. The (3–parameter) Dehnen model does better, providing a good match to the density profiles of large early-type galaxies with Sérsic indices around 4 and greater, but it fails to adequately match the deprojected light–profiles of galaxies with low Sérsic indices, which would encompass dwarf elliptical galaxies and most bulges in disk galaxies (e.g., Balcells et al. 2003, and references therein). If one wishes to explore the hierarchical merging theory, in particular the potential build up of large elliptical galaxies through the collision of lesser elliptical galaxies, then none of the above models are good starting points.

These failures are not particularly surprising because all three of these models were constructed to have outer density profiles that fall off as r^{-4} — in order to match the decline in density of a deprojected $R^{1/4}$ profile. As such, they are highly useful but nonetheless limited models. The (3–parameter) density profile of Prugniel & Simien (1997), however, does not have the above constraint, and consequently does much better, accurately matching the density profiles of luminous elliptical galaxies with $n > 4$ *and* faint ellipticals with $n < 4$, including exponential ($n = 1$) profiles. This model may even prove applicable to the density profiles of ΛCDM–generated dark matter halos.

We have derived exact expressions for the gravitational potential and force associated with the latter density profile. The use of this family of expressions for simulations of elliptical galaxies and bulges in general, and explorations of how their structure may evolve under various circumstances, should enable projects of a nature previously prohibited by the former class of models. Moreover, the equations for the potential and force contain only one elementary function and are otherwise analytical; they are therefore fast to compute.

We have also developed what we believe to be the only density profile capable of simultaneously matching both the nuclear and global stellar distribution in galaxies having partially depleted cores. Application of this (5–parameter) profile to NGC 3348 reveals a good fit (rms ~ 0.03 dex) over 3 orders of magnitude in radial range and 6 in luminosity density. Similar results are obtained from the core galaxies NGC 4291 and NGC 2986. Furthermore, the associated equations for the potential and force are also derived here using only the incomplete gamma function and analytical terms. Expressions to derive the enclosed mass, the spatial and projected velocity dispersion, and the projected intensity profile are additionally provided.

6 ACKNOWLEDGMENTS

We are happy to thank Chris Hunter, Andi Burkert and Agris Kalnajs for their helpful comments and suggestions. We also wish to thank the referee, Eric Emsellem, for his comments on the text. We are grateful to Nicola Caon for providing us with the light–profiles for NGC 1379, 4374, 4458 & 4552, to Peter Erwin for kindly providing us with the light–profile for NGC 3348 and to Massimo Stiavelli for supplying us with the light–profile for LGC 47. This research was supported in part by NSF grant AST-0307351, Department of Energy grant G1A62056 and by NASA grant HST-AR-09927.01-A from the Space Telescope Science Institute, which is operated by the Association of Universities for Research in Astronomy, Inc., under NASA contract NAS5-26555.

REFERENCES

Abramowitz M., Stegun I., 1974, Handbook of Mathematical Functions, Dover: New York
Andredakis, Y.C., & Sanders, R.H. 1994, MNRAS, 267, 283
Baes M., Dejonghe H., Buyle P., 2005, A&A, 432, 411
Balcells M., Graham A.W., Dominguez-Palmero L., Peletier R., 2003, ApJ, 582, L79
Begelman M.C., Blandford R.D., Rees M.J., 1980, Nature, 287, 307
Bertin G., Ciotti L., Del Principe M., 2002, A&A, 386, 149
Binney J., 1980, MNRAS, 190, 873
Binney J., Tremaine S., 1987, Galactic Dynamics, Princeton University Press: Princeton
Caon N., Capaccioli M., Rampazzo R., 1990, A&AS, 86, 429
Caon N., Capaccioli M., D'Onofrio M., 1993, MNRAS, 265, 1013
Cardone V.F., 2004, A&A, 415, 839
Cardone V.F., Piedipalumbo E., Tortora C., 2005, MNRAS, 358, 1325
Ciotti L., 1991, A&A, 249, 99
Cox D.P., 2000, Allen's Astrophysical quantities, New York: AIP Press; Springer, p.341
Dehnen W., 1993, MNRAS, 265, 250
de Jong, R.S. 1996, A&AS, 118, 557
Demarco R., Magnard F., Durret F., Márquez, I., 2003, A&A, 407, 437
de Vaucouleurs G., 1948, Annales d'Astrophysique, 11, 247
de Vaucouleurs G., 1959, in Handbuch der Physik, ed. S.Flügge, Springer, Berlin, p.275
de Vaucouleurs G., Capaccioli M., 1979, ApJS, 40, 669
Erwin P., Graham A.W., Caon N., 2002, in "Carnegie Observatories Astrophysics Series, Vol. 1: Coevolution of Black Holes and Galaxies," ed. L.C. Ho (Pasadena: Carnegie Observatories)
Faber S.M., et al., 1997, AJ, 114, 1771
Ferrarese L., Merritt D., 2000, ApJ, 539, L9
Ferrarese L., van den Bosch F.C., Ford H.C., Jaffe W., O'Connell R.W., 1994, AJ, 108, 1598
Gebhardt K., et al., 1996, AJ, 112, 105
Gebhardt K., et al., 2000, ApJ, 539, L13
Goldstein, H., 1980, Classical Mechanics, Addison-Wesley, Boston
Graham A.W., 2001, AJ, 121, 820
Graham A.W., 2004, ApJ, 613, L33
Graham A.W., Driver, S., 2005, PASA, 22(2), 118

Graham A.W., Erwin P., Caon N., Trujillo I., 2001, ApJ, 563, L11
Graham A.W., Erwin P., Caon N., Trujillo I., 2003a, in Galaxy Evolution: Theory and Observations, RevMexAA (SC), eds., V. Avila-Reese, C. Firmani, C.S. Frenk, & C. Allen, vol.17, p.196-197
Graham A.W., Erwin P., Trujillo I., Asensio Ramos A., 2002, in "Carnegie Observatories Astrophysics Series, Vol. 1: Coevolution of Black Holes and Galaxies," ed. L.C. Ho (Pasadena: Carnegie Observatories: http://www.ociw.edu/ociw/symposia/series/symposium1/proceedings.html)
Graham A.W., Erwin P., Trujillo I., Asensio Ramos A., 2003b, AJ, 125, 2951
Graham A.W., Guzmán R., 2003, AJ, 125, 2936
Graham A.W., Lauer T., Colless M.M., Postman M., 1996, ApJ, 465, 534
Hansen S.H., Moore B., 2005, MNRAS, submitted (astro–ph/0411473)
Hernquist L., 1990, ApJ, 356, 359
Hjorth J., Madsen J., 1995, ApJ, 445, 55
Jaffe W., 1983, MNRAS, 202, 995
Kandrup H.E., Mahon M.E., 1994, Phys. Rev. E 49, 3735
Kandrup H.E., Sideris I.V., Terzić B., Bohn C.L., 2003, ApJ, 597, 111
Kawano Y., Oguri M., Matsubara T., Ikeuchi S., 2004, PASJ, 56, 253
Kormendy J., 1985, ApJ, 295, 73
Kormendy J., Djorgovski S., 1989, ARA&A, 27, 235
Landau, L.D., Lipshitz, E.M., 1976, Mechanics, Butterworth-Heinemann, Burlington, MA
Lauer T.R., 1985, ApJ, 292, 104
Lauer T.R., et al., 1995, AJ, 110, 2622
Lima Neto G.B., Gerbal D., Márquez I., 1999, MNRAS, 309, 481
MacArthur, L.A., Courteau, S., & Holtzman, J.A. 2003, ApJ, 582, 689
Magorrian J., et al., 1998, AJ, 115, 2285
Makino J., Ebisuzaki T., 1996, ApJ, 465, 527
Makino J., Funato Y., 2004, ApJ, 602, 93
Márquez I., Lima Neto G.B., Capelato H., Durret F., Gerbal D., 2000, 353, 873
Márquez I., Lima Neto G.B., Capelato H., Durret F., Lanzoni B., Gerbal D., 2001, A&A, 379, 767
Mazure A., Capelato H.V., 2002, A&A, 383, 384
McLure R.J., Dunlop J.S., 2002, MNRAS, 331, 795
Mellier Y., Mathez G., 1987, A&A, 175, 1
Merritt D., 2004, in "Growing Black Holes: Accretion in Cosmological Context" (astro–ph/0409290)
Merritt D., Fridman T., 1996, ApJ, 460, 136
Merritt D., Navarro J.F., Ludlow A., Jenkins A., 2005, ApJL, 624, L85
Merritt D., Poon M.Y., 2004, ApJ, 606, 788
Merritt D., Valluri M., 1996, ApJ, 471, 82
Milosavljević M., Merritt D., 2001, ApJ, 563, 34
Milosavljević M., Merritt D., 2005, in "Living Reviews in Relativity" (astro–ph/0410364)
Milosavljević, M., Merritt, D., Rest, A., & van den Bosch, F.C. 2002, MNRAS, 331, L51
Navarro J.F., Frenk C.S., White S.D.M., 1996, ApJ, 462, 563
Navarro J.F., Frenk C.S., White S.D.M., 1997, ApJ, 490, 493
Navarro J.F., Hayashi E., Power C., Jenkins A.R., Frenk C.S., 2004, MNRAS, 349, 1039
Poon M.Y., Merritt D., 2002, ApJ, 568, L89
Poon M.Y., Merritt D., 2004, ApJ, 606, 774
Prugniel Ph., Simien F., 1997, A&A, 321, 111
Ravindranath, S., Ho, L.C., & Filippenko, A.V. 2002, ApJ, 566, 801
Rest A., et al., 2001, AJ, 121, 2431
Sérsic J.-L., 1963, Boletin de la Asociacion Argentina de Astronomia, vol.6, p.41
Sérsic J.L., 1968, Atlas de galaxias australes
Simonneau, E., Prada, F., 2004, RevMexAA, 40, 69
Siopis C.V., Kandrup H.E., 2000, MNRAS, 319, 43
Stiavelli M., Miller B.W., Ferguson H.C., Mack J., Whitmore B.C., Lotz J.M., 2001, AJ, 121, 1385
Terzić B., 2003, ApJ, submitted (astro-ph/0305005)
Terzić B., Kandrup H.E., 2004, MNRAS, 347, 957
Tonry J., Blakeslee J.P., Ajhar E.A., Dressler A., 1997, ApJ, 475, 399
Tremaine S., et al., 1994, AJ, 107, 634
Trenti M., Bertin G., 2005, A&A, 429, 161
Trujillo I., Asensio Ramos A., Rubiño-Martin J.A., Graham A.W., Aguerri J.A.L., Cepa J., Gutiérrez C.M., 2002, MNRAS, 333, 510
Trujillo I., Erwin P., Asensio Ramos A., Graham A.W. 2004, AJ, 127, 1917
Young C.K., Currie M.J., 1994, MNRAS, 268, L11
Zhao H.S., 1996, MNRAS, 278, 488

7 APPENDIX A: MASS, CIRCULAR VELOCITY, AND VELOCITY DISPERSION

7.1 Prugniel–Simien density profile

In this section we provide some additional helpful expressions related to the density profile $\rho(r)$ given in Prugniel & Simien (1997, their equation B6), and given here by equation (4).

Assuming spherical symmetry, the enclosed mass, $M(r)$, is simply

$$M(r) = 4\pi \int_0^r \rho(\bar{r})\bar{r}^2 \, d\bar{r}. \tag{24}$$

Using the change of variable $\bar{Z} = b(\bar{r}/R_e)^{1/n}$, such that $d\bar{r} = R_e n b^{-n} \bar{Z}^{n-1} d\bar{Z}$, one obtains

$$M(r) = 4\pi\rho_0 {R_e}^3 n b^{n(p-3)} \gamma\left(n(3-p), Z\right), \tag{25}$$

where $Z = b(r/R_e)^{1/n}$ and $\gamma(a, x)$ is the incomplete gamma function given in equation (2). The total mass is obtained by replacing $\gamma\left(n(3-p), Z\right)$ with $\Gamma\left(n(3-p)\right)$.

The circular velocity is given by

$$v_{\rm circ}(r) = \sqrt{\frac{GM(r)}{r}}. \tag{26}$$

Assuming isotropy, the spatial velocity dispersion is given in Binney (1980) as

$$\begin{aligned} {\sigma_s}^2(r) &= \frac{G}{\rho(r)} \int_r^\infty \rho(\bar{r}) \frac{M(\bar{r})}{\bar{r}^2} d\bar{r} \\ &= \frac{4\pi G {\rho_0}^2 {R_e}^2 n^2 b^{2n(p-1)}}{\rho(r)} \int_Z^\infty \bar{Z}^{-n(p+1)-1} e^{-\bar{Z}} \gamma\left(n(3-p), \bar{Z}\right) d\bar{Z}. \end{aligned} \tag{27}$$

This expression is easily computed numerically after making the substitution $\bar{Z} = (Z/\cos\theta)$, such that $d\bar{Z}/d\theta = Z\sin\theta/\cos^2\theta$, giving

$${\sigma_s}^2(r) = \frac{4\pi G(\rho_0 R_e n b^{n(p-1)})^2 Z^{-n(p+1)}}{\rho(r)} \int_0^{\pi/2} \tan\theta(\cos\theta)^{n(p+1)} e^{-Z/\cos\theta} \gamma\left(n(3-p), \frac{Z}{\cos\theta}\right) d\theta. \tag{28}$$

The projected, line–of–sight velocity dispersion as given by equation (B12) in Prugniel & Simien (1997) is

$$\begin{aligned} {\sigma_p}^2(R) &= \frac{2G}{I(R)M_{\rm tot}} \int_R^\infty \frac{\sqrt{\bar{r}^2 - R^2}}{\bar{r}^2} \rho(\bar{r}) M(\bar{r}) \, d\bar{r} \\ &= \frac{8\pi G {\rho_0}^2 {R_e}^3 n^2 b^{n(2p-3)}}{I(R)M_{\rm tot}} \int_Z^\infty \sqrt{\bar{Z}^{2n} - Z^{2n}} \; \bar{Z}^{-n(p+1)-1} e^{-\bar{Z}} \gamma\left(n(3-p), \bar{Z}\right) d\bar{Z} \\ &= \frac{8\pi G {\rho_0}^2 {R_e}^3 n^2 b^{n(2p-3)}}{I(R)M_{\rm tot}} Z^{-np} \int_0^{\pi/2} \sqrt{1 - (\cos\theta)^{2n}} \tan\theta(\cos\theta)^{np} e^{-Z/\cos\theta} \gamma\left(n(3-p), \frac{Z}{\cos\theta}\right) \end{aligned} \tag{29}$$

with Z now equal to $b(R/R_e)^{1/n}$.

The mass profiles, circular velocity profiles, spatial and projected velocity dispersion profiles are shown in Fig. 11 for a range of profile shapes. They agree closely with those obtained from the exact deprojection of Sérsic's $R^{1/n}$ model (Ciotti 1991; Simonneau & Prada 2004). In order to show the behavior of $v_{\rm circ}$ near the break radius r_b, and to allow comparisons of $(v_{\rm circ})^2$ with σ^2, we present both $v_{\rm circ}$ on a logarithmic scale and $(v_{\rm circ})^2$ on a linear scale.

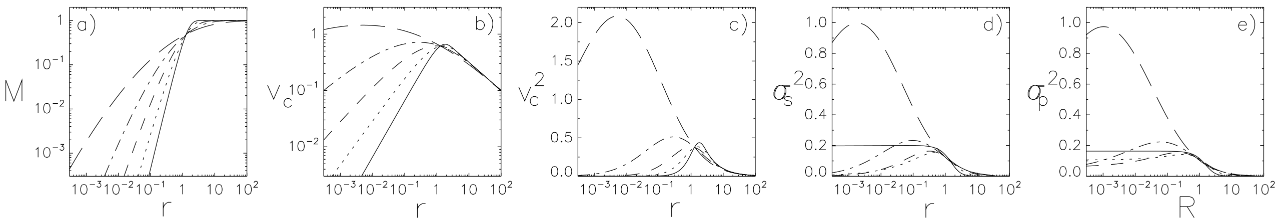

Figure 11. Core–less galaxies. Panel a) mass (equation 25), b) circular velocity (equation 26), c) circular velocity squared, d) spatial velocity dispersion squared (equation 27), and e) the square of the projected, line–of–sight velocity dispersion (equation 29), for varying values of the profile shape n: $n = 0.5$ (solid lines), $n = 1$ (dotted), $n = 2$ (dashed), $n = 4$ (dash-dot), $n = 10$ (double–dash). We have set R_e=1, $M_{tot} = 1$, and $G = 1$. The square of each velocity term is thus effectively normalised to GM_{tot}/R_e. Spherical symmetry and isotropy have been assumed.

7.2 Our density profile

Below are the equivalent expressions relevant to our adaptation of Prugniel & Simien's density profile for galaxies with power–law cores.

The enclosed mass $M(r)$ is

$$M(r) = 4\pi \int_0^r \rho(\bar{r})\bar{r}^2\, d\bar{r} = 4\pi \int_0^{r_{\rm min}} \rho_1(\bar{r})\bar{r}^2\, d\bar{r} + 4\pi \int_{r_{\rm min}}^{r} \rho_2(\bar{r})\bar{r}^2\, d\bar{r} \equiv M_1(r) + M_2(r) \tag{30}$$

where $\rho_1(\bar{r})$ and $\rho_2(\bar{r})$ are given in equation (17), $r_{\rm min}$ is the minimum value of r or r_b, and

$$M_1(r) = 4\pi J_1(r), \tag{31}$$

$$M_2(r) = 4\pi L_2(r), \tag{32}$$

where $J_1(r)$ and $L_2(r)$ are defined in equations (9) and (12), respectively. The total mass is obtained by setting the second incomplete gamma function in the expression for $L_2(r)$ (equation 12) equal to zero. Assuming spherical symmetry, the circular velocity is given by equation (26).

Again assuming isotropy, the spatial velocity dispersion is given by

$$\sigma_{\rm s}{}^2(r) \equiv K_1(r) + K_2(r) + K_3(r), \tag{33}$$

where

$$\begin{aligned} K_1(r) &= \frac{G}{\rho_1(r)} \int_r^{r_{\rm max}} \rho_1(\bar{r}) \frac{M_1(\bar{r})}{\bar{r}^2} d\bar{r} \\ &= \frac{4\pi G {\rho_b}^2 {r_b}^{2\gamma}}{\rho_1(r)} \begin{cases} \frac{1}{3-\gamma} \ln \frac{r_{\rm max}}{r} & \text{if } \gamma = 1 \\ \frac{1}{2(3-\gamma)(1-\gamma)} \left({r_{\rm max}}^{2(1-\gamma)} - r^{2(1-\gamma)} \right) & \text{if } \gamma \neq 1 \text{ and } < 3 \end{cases}, \end{aligned} \tag{34}$$

$$\begin{aligned} K_2(r) &= \frac{G}{\rho_2(r)} M_1(r_b) \int_{r_{\rm max}}^{\infty} \frac{\rho_2(\bar{r})}{\bar{r}^2} d\bar{r} \\ &= \frac{G M_1(r_b) \rho_b \bar{\rho} n b^{n(p+1)}}{R_{\rm e} \rho_2(r)} \int_{Z_{\rm max}}^{\infty} \bar{Z}^{-n(p+1)-1} e^{-\bar{Z}} d\bar{Z}, \end{aligned} \tag{35}$$

$$\begin{aligned} K_3(r) &= \frac{G}{\rho_2(r)} \int_{r_{\rm max}}^{\infty} \rho_2(\bar{r}) \frac{M_2(\bar{r})}{\bar{r}^2} d\bar{r} \\ &= \frac{4\pi G {\rho_b}^2 \bar{\rho}^2 {R_{\rm e}}^2 n^2 b^{2n(p-1)}}{\rho_2(r)} \end{aligned}$$

$$\times \int_{Z_{\max}}^{\infty} \bar{Z}^{-n(p+1)-1} e^{-\bar{Z}} \left[\Gamma\left(n(3-p), Z_b\right) - \Gamma\left(n(3-p), \bar{Z}\right)\right] d\bar{Z}, \tag{36}$$

with $r_{\max} = \max(r, r_b)$, $Z = b(r/R_e)^{1/n}$, $Z_b = b(r_b/R_e)^{1/n}$ and $Z_{\max} = \max(Z, Z_b)$. In passing, we note that the term $-n(p+1)$ appearing in the expression for $K_2(r)$ equals $0.6097 - 2n - 0.05563/n$, and is thus negative for values of n greater than about 0.2. For this reason we did not express $K_2(r)$ in terms of the incomplete gamma function. Following what was done with equation (27), to help evaluate $K_2(r)$ and $K_3(r)$ numerically one may apply the change of variable $\bar{Z} = Z_{\max}/\cos\theta$, to give

$$K_2(r) = \frac{GM_1(r_b)\rho_b\bar{\rho}nb^{n(p+1)}}{R_e\rho_2(r)}(Z_{\max})^{-n(p+1)} \int_0^{\pi/2} \tan\theta(\cos\theta)^{n(p+1)} e^{-Z_{\max}/\cos\theta} d\theta, \tag{37}$$

$$\begin{aligned} K_3(r) &= \frac{4\pi G{\rho_b}^2\bar{\rho}^2{R_e}^2 n^2 b^{2n(p-1)}}{\rho_2(r)}(Z_{\max})^{-n(p+1)} \\ &\times \int_0^{\pi/2} \tan\theta(\cos\theta)^{n(p+1)} e^{-Z_{\max}/\cos\theta} \left[\Gamma\left(n(3-p), Z_b\right) - \Gamma\left(n(3-p), Z_{\max}/\cos\theta\right)\right] d\theta. \end{aligned} \tag{38}$$

Alternatively, one may use the change of variable $\bar{r} = 1/s$ to transform the $K_2(r)$ term into the expression

$$K_2(r) = \frac{G}{\rho_2(r)} M_1(r_b) \int_0^{1/r_{\max}} \rho_2(1/s) ds. \tag{39}$$

The projected, line–of–sight velocity dispersion is found to be

$${\sigma_p}^2(R) \equiv S_1(R) + S_2(R) + S_3(R), \tag{40}$$

where

$$\begin{aligned} S_1(R) &= \frac{2G}{I(R)M_{\rm tot}} \int_R^{R_{\max}} \frac{\sqrt{\bar{r}^2 - R^2}}{\bar{r}^2} \rho_1(\bar{r}) M_1(\bar{r})\, d\bar{r} \\ &= \frac{8\pi G{\rho_b}^2{r_b}^{2\gamma}{R_e}^{3-2\gamma} nb^{n(2\gamma-3)}}{I(R)M_{\rm tot}(3-\gamma)} \int_Z^{Z_{\max}} \sqrt{\bar{Z}^{2n} - Z^{2n}}\, \bar{Z}^{2n(1-\gamma)-1} d\bar{Z} \quad \text{if } \gamma < 3, \end{aligned} \tag{41}$$

$$\begin{aligned} S_2(R) &= \frac{2G}{I(R)M_{\rm tot}} M_1(r_b) \int_{R_{\max}}^{\infty} \frac{\sqrt{\bar{r}^2 - R^2}}{\bar{r}^2} \rho_2(\bar{r})\, d\bar{r} \\ &= \frac{2G}{I(R)M_{\rm tot}} M_1(r_b) nb^{np}\rho_b\bar{\rho} \int_{Z_{\max}}^{\infty} \sqrt{\bar{Z}^{2n} - Z^{2n}}\, \bar{Z}^{-n(p+1)-1} e^{-\bar{Z}} d\bar{Z}, \end{aligned} \tag{42}$$

$$\begin{aligned} S_3(R) &= \frac{2G}{I(R)M_{\rm tot}} \int_{R_{\max}}^{\infty} \frac{\sqrt{\bar{r}^2 - R^2}}{\bar{r}^2} \rho_2(\bar{r}) M_2(\bar{r})\, d\bar{r} \\ &= \frac{8\pi G{\rho_b}^2\bar{\rho}^2{R_e}^3 n^2 b^{n(2p-3)}}{I(R)M_{\rm tot}} \\ &\times \int_{Z_{\max}}^{\infty} \sqrt{\bar{Z}^{2n} - Z^{2n}}\, \bar{Z}^{-n(p+1)-1} e^{-\bar{Z}} \left[\Gamma\left(n(3-p), Z_b\right) - \Gamma\left(n(3-p), \bar{Z}\right)\right] d\bar{Z}, \end{aligned} \tag{43}$$

with $R_b = r_b$, $R_{\max}$ =max(R, R_b), $Z = b(R/R_e)^{1/n}$ and $Z_b = b(R_b/R_e)^{1/n}$. Equation 42 and 43 can be integrated numerically using the change of variable $\bar{Z} = Z_{\max}/\cos\theta$.

The mass profiles, circular velocity profiles, spatial and projected velocity dispersion profiles are shown in Fig. 12 for a range of profile shapes. The intriguing "dip" in some of the

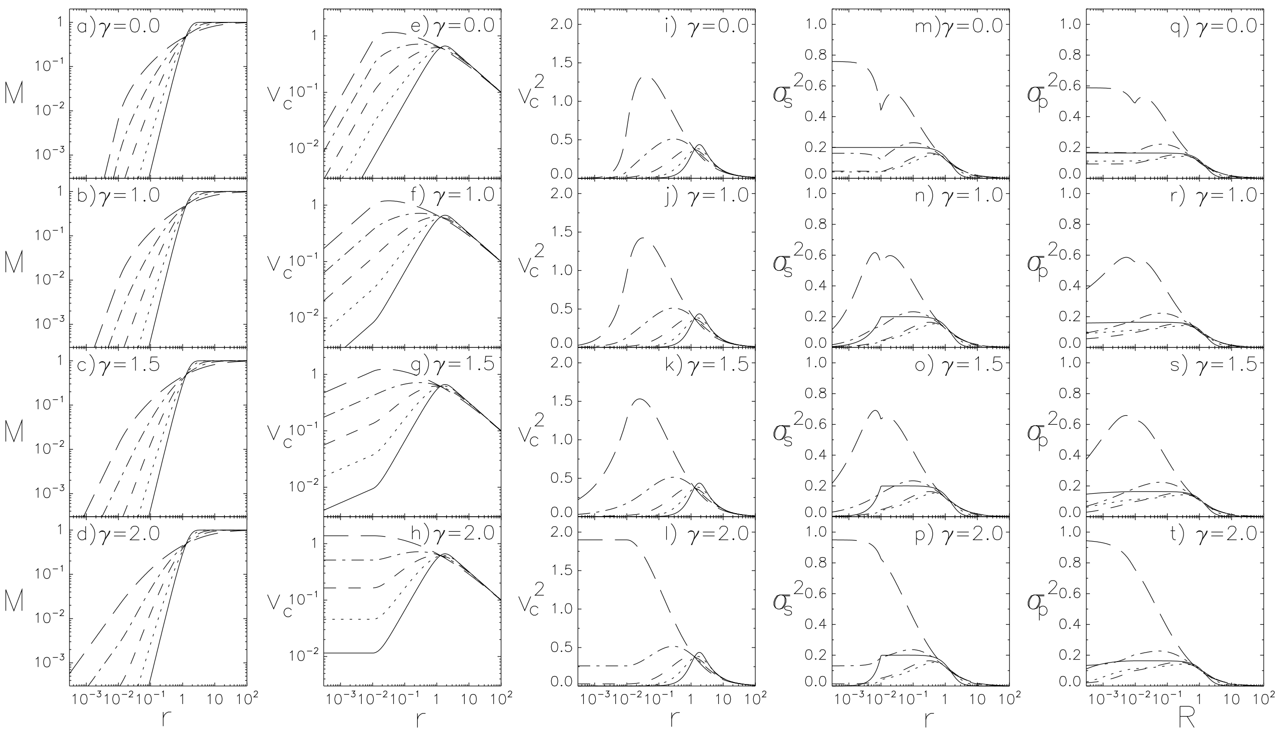

Figure 12. Core galaxies. Panels a–d) show the normalised mass (equation 30), e–h) circular velocity (equation 26), i–l) circular velocity squared, m–p) spatial velocity dispersion squared (equation 33) and q–t) the square of the projected, line–of–sight velocity dispersion (equation 40), for varying values of the outer profile shape n: $n = 0.5$ (solid lines), $n = 1$ (dotted), $n = 2$ (dashed), $n = 4$ (dash-dot), $n = 10$ (double–dash); and varying central cusp slope γ. We have set $R_e = 1$, $r_b = 0.01$, $M_{tot} = 1$, and $G = 1$. The square of each velocity term is thus effectively normalised to GM_{tot}/R_e. Spherical symmetry and isotropy have been assumed. To show the behavior of v_{circ} near r_b, and to enable easy comparison of $(v_{circ})^2$ with σ_s^2 and σ_p^2, we present v_{circ} on a logarithmic scale and $(v_{circ})^2$ on a linear scale.

velocity dispersion profiles, most notably the high n profiles with small γ, is perhaps worth commenting on. It arises from the use of a sharp transition in the density profile (equation 6) when the inner and outer slope (on either side of r_b) are markedly different. Application of a model with an extended transition region quenches this dip. The use of equation 5 with decreasing values of α, i.e. an increasingly broader transition region, steadily reduces and eliminates the dip. While profiles with $\alpha = 10$ largely reproduce the velocity dispersions shown, density profiles with $\alpha = 1$ have smooth velocity dispersion profiles. In any case, an inspection of the "pseudo" potential (equation 15) reveals that such a velocity structure does not give rise to an unstable situation for particle orbits.

Equations pertaining to Prugniel & Simien's (1997) density profile are obtained by setting $r_b = 0$ and $\rho_b \bar{\rho} = \rho_0$. Indeed, upon making these substitutions in the derivation of equations for enclosed mass and velocity dispersion above, $r_{min} = 0$, $r_{max} = r$, $R_{max} = R$, $Z_{max} = Z$ and the terms $K_1(r)$, $K_2(r)$, $S_1(r)$ and $S_2(r)$ vanish. Equations (25), (27) and (29) are then easily recovered.

8 APPENDIX B: DERIVATION OF THE POTENTIAL, FORCE AND INTENSITY PROFILES

8.1 Potential

If the expression for the density (equation 6) is rewritten as $\rho(r) = \rho_1(r) + \rho_2(r)$ (as was done in subsection 2.3, equation 17), then the potential (equation 7) can be written as

$$\Phi(r) = -4\pi G \begin{cases} \frac{1}{r}\int\limits_0^r \rho_1(\bar{r})\bar{r}^2\, d\bar{r} + \int\limits_r^{r_b} \rho_1(\bar{r})\bar{r}\, d\bar{r} + \int\limits_{r_b}^{\infty} \rho_2(\bar{r})\bar{r}\, d\bar{r} & \text{if } r \le r_b, \\ \frac{1}{r}\int\limits_0^{r_b} \rho_1(\bar{r})\bar{r}^2\, d\bar{r} + \frac{1}{r}\int\limits_{r_b}^{r} \rho_2(\bar{r})\bar{r}^2\, d\bar{r} + \int\limits_r^{\infty} \rho_2(\bar{r})\bar{r}\, d\bar{r} & \text{if } r > r_b, \end{cases} . \tag{44}$$

$$\Phi(r) = -4\pi G \begin{cases} \frac{1}{r}J_1(r) + J_2(r) + L_1(r_b) & \text{if } r \le r_b, \\ \frac{1}{r}J_1(r_b) + \frac{1}{r}L_2(r) + L_1(r) & \text{if } r > r_b, \end{cases} , \tag{45}$$

The derivation of integrals $J_1(r)$ and $J_2(r)$, which only involve a power-law integrand associated with $\rho_1(r)$, is trivial, while the integrals which involve $\rho_2(r)$ require a change of variable $\bar{Z} \equiv b(\bar{r}/R_{\rm e})^{1/n}$, so that $\bar{r} = R_{\rm e}(\bar{Z}/b)^n$ and $d\bar{r} = R_{\rm e} n \bar{Z}^{n-1} b^{-n} d\bar{Z}$:

$$\begin{aligned} L_1(r) &\equiv \int\limits_r^{\infty} \rho_2(\bar{r})\bar{r}\, d\bar{r} = \rho_b\bar{\rho} \int\limits_r^{\infty} \left(\frac{\bar{r}}{R_{\rm e}}\right)^{-p} {\rm e}^{-b(\bar{r}/R_{\rm e})^{1/n}}\bar{r}\, d\bar{r} \\ &= \rho_b\bar{\rho}R_{\rm e} \int\limits_r^{\infty} \left(\frac{\bar{r}}{R_{\rm e}}\right)^{1-p} {\rm e}^{-b(\bar{r}/R_{\rm e})^{1/n}}\, d\bar{r} \\ &= \rho_b\bar{\rho}{R_{\rm e}}^2 n b^{n(p-2)} \int\limits_{b(r/R_{\rm e})^{1/n}}^{\infty} \bar{Z}^{n(2-p)-1}{\rm e}^{-\bar{Z}}\, d\bar{Z} \\ &= \rho_b\bar{\rho}{R_{\rm e}}^2 n b^{n(p-2)} \Gamma\left(n(2-p), b\left(\frac{r}{R_{\rm e}}\right)^{1/n}\right) \end{aligned} \tag{46}$$

$$\begin{aligned} L_2(r) &\equiv \int\limits_{r_b}^{r} \rho_2(\bar{r})\bar{r}^2\, d\bar{r} = \rho_b\bar{\rho} \int\limits_{r_b}^{r} \left(\frac{\bar{r}}{R_{\rm e}}\right)^{-p} {\rm e}^{-b(\bar{r}/R_{\rm e})^{1/n}}\bar{r}^2\, d\bar{r} \\ &= \rho_b\bar{\rho}{R_{\rm e}}^2 \int\limits_{r_b}^{r} \left(\frac{\bar{r}}{R_{\rm e}}\right)^{2-p} {\rm e}^{-b(\bar{r}/R_{\rm e})^{1/n}}\, d\bar{r} \\ &= \rho_b\bar{\rho}{R_{\rm e}}^3 n b^{n(p-3)} \int\limits_{b(r_b/R_{\rm e})^{1/n}}^{b(r/R_{\rm e})^{1/n}} \bar{Z}^{n(3-p)-1}{\rm e}^{-\bar{Z}}\, d\bar{Z} \\ &= \rho_b\bar{\rho}{R_{\rm e}}^3 n b^{n(p-3)} \left[\Gamma\left(n(3-p), b\left(\frac{r_b,}{R_{\rm e}}\right)^{1/n}\right) - \Gamma\left(n(3-p), b\left(\frac{r}{R_{\rm e}}\right)^{1/n}\right)\right]. \end{aligned} \tag{47}$$

8.2 Force

Computing the radial force requires differentiation of the potential (8) with respect to the radial coordinate r. When $r \le r_b$, the differentiation is trivial after realising that the last term is constant. For $r > r_b$, we use the relation given in Abramowitz & Stegun (1974, their equation 6.5.25):

$$\frac{\partial\Gamma(a,x)}{\partial x} = -x^{a-1}{\rm e}^{-x}, \tag{48}$$

and we note the following cancellation of terms simplifies matters

$$\frac{1}{r}\frac{dL_2(r)}{dr} = -\frac{dL_1(r)}{dr} = \rho_b \bar{\rho} R_\mathrm{e} \left(\frac{r}{R_\mathrm{e}}\right)^{1-p} \mathrm{e}^{-b(r/R_\mathrm{e})^{1/n}}. \qquad (49)$$

8.3 Projected Intensity

Substituting $\rho_1(r)$ from equation (17) into equation (16) yields

$$I_1(R) = \frac{2}{\Upsilon}\rho_b {r_b}^\gamma \int_R^{r_b} \frac{r^{1-\gamma}}{\sqrt{r^2 - R^2}} dr. \qquad (50)$$

By using the change of variable $y = r^2$, it is trivial to compute the expression for the special case when $\gamma = 0$. The solution is given in the first line of equation (19).

When $\gamma = 1$, the change of variable $r = R/\cos\theta$, such that $dr/d\theta = R\sin\theta/\cos^2\theta$, gives

$$\begin{aligned} I_1(R) &= \frac{2}{\Upsilon}\rho_b {r_b}^\gamma \int_R^{r_b} \frac{1}{\sqrt{r^2 - R^2}} dr = \frac{2}{\Upsilon}\rho_b {r_b}^\gamma \int_0^{\cos^{-1}(R/r_b)} \frac{1}{\cos\theta} d\theta \\ &= \frac{2}{\Upsilon}\rho_b {r_b}^\gamma \ln\left(\frac{1}{\cos\theta} + \frac{\sin\theta}{\cos\theta}\right)\Bigg|_0^{\cos^{-1}(R/r_b)} = \frac{2}{\Upsilon}\rho_b {r_b}^\gamma \ln\left(\frac{1+\sqrt{1-\cos^2\theta}}{\cos\theta}\right)\Bigg|_0^{\cos^{-1}(R/r_b)} \\ &= \frac{2}{\Upsilon}\rho_b {r_b}^\gamma \ln\left(\frac{1+\sqrt{1-R^2/{r_b}^2}}{R/r_b}\right) = \frac{2}{\Upsilon}\rho_b {r_b}^\gamma \ln\left(\frac{r_b+\sqrt{r_b^2-R^2}}{R}\right). \end{aligned} \qquad (51)$$

For other values of the cusp slope γ, further transformation of equation (50) is required. Using the change of variable $y \equiv 1 - R^2/r^2$, equation (50) becomes

$$\begin{aligned} I_1(R) &= \frac{2}{\Upsilon}\rho_b {r_b}^\gamma \left[\frac{1}{2}R^{1-\gamma} \int_0^{1-R^2/{r_b}^2} y^{-1/2}(1-y)^{(\gamma-3)/2} dy\right] \\ &= \frac{\rho_b {r_b}^\gamma}{\Upsilon} R^{1-\gamma} B_{1-R^2/{r_b}^2}\left(\frac{1}{2}, \frac{\gamma-1}{2}\right). \end{aligned} \qquad (52)$$

When $\gamma = 2$, the incomplete beta function (equation 20) can be simplified through the change of variable $u = t^2$, to give

$$I_1(R) = \frac{2}{\Upsilon}\rho_b {r_b}^\gamma \left[R^{-1} \int_0^{\sqrt{1-R^2/{r_b}^2}} \frac{1}{\sqrt{1-t^2}} dt\right] = \frac{2\rho_b {r_b}^\gamma}{\Upsilon} R^{-1} \sin^{-1}\left(\sqrt{1-R^2/r_b^2}\right). \qquad (53)$$